

Active Targeting of Block Copolymer Micelles with Trastuzumab Fab Fragments and Nuclear Localization Signal Leads to Increased Tumor Uptake and Nuclear Localization in HER2-Overexpressing Xenografts

Bryan Hoang,^{†,¶} Sandra N. Ekdawi,^{†,¶} Raymond M. Reilly,^{†,§,||} and Christine Allen^{*,†,‡,⊥}

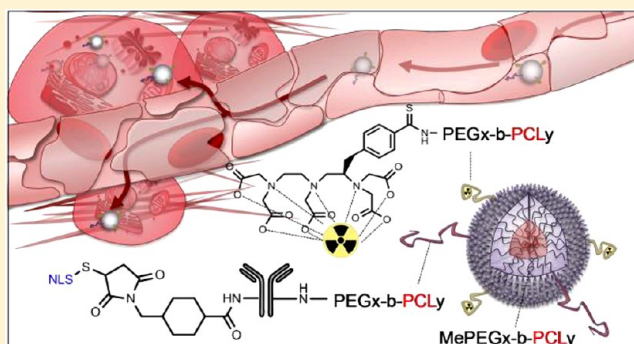
[†]Leslie Dan Faculty of Pharmacy, [‡]Department of Chemistry, and [§]Department of Medical Imaging, University of Toronto, 144 College St., Toronto, Ontario, M5S 3M2, Canada

^{||}Toronto General Research Institute, University Health Network, 200 Elizabeth St., Toronto, Ontario, M5G 2C4, Canada

[⊥]STTARR Innovation Centre, Radiation Medicine Program, Princess Margaret Hospital, University Health Network, 610 University Ave, Toronto, Ontario, M5T 2M9, Canada

ABSTRACT: Block copolymer micelles (BCMs) have been employed as effective drug delivery systems to solid tumors by virtue of their capacity to transport large therapeutic payloads and passively target tumor sites. Active targeting of nanoparticles (NPs) has been exploited as a means to increase the therapeutic efficacy of NP-based drugs by promoting their delivery to cellular sites of action. Effective whole tumor accumulation and cellular uptake constitute key objectives in the success of preclinical drug formulations, although they have seldom been investigated concurrently *in vivo*. The current study aims to elucidate the *in vivo* fate of 31-nm-sized block copolymer micelles (BCMs) targeted to the nucleus of HER2-overexpressing breast cancer cells. Pharmacokinetics, biodistribution, tumor uptake, and intratumoral distribution of BCMs were investigated in mice bearing subcutaneous BT-474 and MDA-MB-231 xenografts expressing high and low levels of HER2, respectively. Radiolabeling with ¹¹¹indium enabled quantitative assessment of BCM distribution at the whole body, tissue, and cellular levels. Surface-grafted trastuzumab Fab fragments (TmAb-Fab) facilitated binding and internalization of BCMs by HER2-positive breast cancer cells, while synthetic 13-mer nuclear localization signal (NLS) peptides conjugated to the TmAb-Fab conferred nuclear translocation capability. Active targeting of BCMs led to a 5-fold increase in tumor uptake in HER2-overexpressing BT-474 tumors, alongside a correspondingly greater level of cellular uptake and nuclear localization, relative to the nontargeted formulations. This study distinctively highlights the quantitative evaluation of active targeting on tumor, cellular and subcellular uptake of BCMs and presents a promising platform for the effective delivery of chemo- and/or radiotherapy *in vivo*.

KEYWORDS: nanotechnology, block copolymer micelles, active targeting, HER2



INTRODUCTION

The use of polymeric micelles as functional reservoirs for site-specific delivery of drugs has been well-established with numerous formulations in late stage clinical development.^{1–4} The size and colloidal stability of block copolymer micelles (BCMs) enables their extended systemic circulation, relative to small molecules.^{5–7} Prolonged circulation of nanosystems in the blood favors their accumulation and retention within solid tumors via the enhanced permeability and retention effect (EPR).^{8,9} Leveraging on this phenomenon, nanoparticles (NPs) have been utilized to improve drug deposition through passive targeting at the tumor site, resulting in levels up to 10- to 100-fold higher than that achieved following administration of the free drug.¹⁰

Receptor-based or active targeting of NPs to antigens associated with neoplastic tissues has been exploited in an effort to promote cellular uptake of the delivered therapeutic.

However, the influence of targeting moieties on the distribution of NPs, in particular BCMs, at the whole body, tumor, and cellular levels has yet to be fully elucidated. A review of the literature reveals that the influence of a targeting ligand on the pharmacokinetics, biodistribution, and tumor accumulation of NPs depends on the nature of the ligand,¹¹ its density at the surface of the NP,¹² as well as the presence and properties of the PEG steric stabilizing layer.^{12–14} In particular, it is vital that the addition of the targeting moiety does not impair the circulation lifetime of the NP by promoting mononuclear phagocyte system (MPS)-mediated clearance and, thus, reduced tumor accumulation and efficacy.^{11,12,15} Nevertheless,

Received: May 25, 2013

Revised: September 3, 2013

Accepted: September 25, 2013

Published: September 25, 2013

while improved tumor accumulation constitutes a valuable prerequisite for NP-based drug delivery, it may prove to be insufficient in terms of determining the performance of NPs as efficacious drug delivery systems.¹⁶ Indeed, it has been shown that an increase in efficacy resulting from the administration of an actively targeted NP formulation is not necessarily associated with an increase in tumor accumulation relative to the nontargeted formulation.^{17–20} A key study conducted by Kirpotin et al. has demonstrated that superior antitumor efficacy achieved using an actively targeted liposome formulation was due to greater tumor cell uptake *in vivo*.¹⁷ Specifically, HER2-targeted liposomes bearing anti-HER2 Fab' monoclonal antibody fragments did not localize to a greater extent within HER2-overexpressing breast cancer tumor xenografts relative to the nontargeted liposomes. The enhanced antitumor effect observed with the targeted formulation was effectively attributed to the 6-fold increase in tumor cell uptake resulting from HER2-mediated internalization.¹⁷

HER2 gene amplification and/or HER2 protein overexpression have been reported in approximately 20% of breast cancers (BCs)^{21,22} and are often associated with an increased risk of locoregional recurrence and death.^{23–26} Recent studies by our groups have evaluated BCMs and macromolecular agents for delivery of the Auger electron emitter indium-111 (¹¹¹In) for radiotherapy of BC.^{27–29} Owing to the relatively short nanometer-to-micrometer range of the Auger electrons, the damage incurred by the tumor cell is greatest when ¹¹¹In is delivered within proximity of the nucleus.³⁰ Previously, BCMs labeled with the Fab fragment of the monoclonal antibody trastuzumab (Herceptin, TmAb-Fab) and conjugated with nuclear localization signal (NLS) peptides were developed for targeting HER2-overexpressing BC cells.²⁹ The receptor binding affinity and *in vitro* cell uptake, as well as subcellular distribution and cytotoxicity (i.e., by clonogenic survival) of the ¹¹¹In-labeled and NLS₂-TmAb-Fab-conjugated BCMs (¹¹¹In/NLS₂-TmAb-Fab-BCMs), were examined in a panel of BC cell lines with varying levels of HER2 expression.²⁹ The ¹¹¹In/NLS₂-TmAb-Fab-BCMs were internalized by receptor-mediated endocytosis, and approximately 43% of the internalized population was successfully transported to the nucleus of cells expressing high levels of HER2.²⁹ Nuclear transport was effectively facilitated by the conjugated NLS domain, which enables active transport of macromolecules that are larger than the 9 nm threshold required for passive diffusion across the nuclear pore complexes (NPC).³¹ Moreover, the ¹¹¹In/NLS₂-TmAb-Fab-BCMs were effective at killing BC cells with high HER2 receptor density.²⁹ We have sought to translate these findings *in vivo*, recognizing the vital need to both challenge and extend the results of *in vitro* studies in animal models.^{16,32} In particular, effective delivery to the target site of action has been seemingly undervalued in preclinical studies. In this work, we have performed a quantitative evaluation of BCM uptake in mice bearing BC tumor xenografts with varying levels of HER2 expression. Notably, the impact of active targeting with TmAb-Fab and NLS was assessed on the respective cellular uptake and nuclear localization of the BCMs *in vivo*.

■ EXPERIMENTAL PROCEDURES

Materials. Triethylamine, hydrochloric acid (1 M, HCl in ether), *N*-Hydroxysuccinimide (NHS), dimethyl sulfoxide (DMSO), *N,N'*-Dicyclohexylcarbodiimide (DCC), and *N,N*-Dimethylformamide (DMF) were purchased from Sigma-Aldrich (Oakville, ON). Methoxy poly(ethylene glycol)

(MePEG, $M_n = 3000$, $M_w/M_n = 1.06$), was purchased from Polymer Source Inc. (Montreal, QC). Heterobifunctional α -hydroxy- ω -amino poly(ethylene glycol) (HO-PEG-NH₂, $M_n = 3000$, $M_w/M_n = 1.08$) was purchased from Jenkem Technology Inc. (Beijing, China), and α -carboxy- ω -hydroxy poly(ethylene glycol) (HOOC-PEG-NH₂, $M_n = 3300$, $M_w/M_n = 1.08$) was synthesized by a thiol-anionic polymerization method as previously described.³³ 2-(4-Isothiocyanatobenzyl)-diethylenetriaminepentaacetic acid (*p*-SCN-Bn-DTPA) was purchased from Macrocyclics Inc. (Dallas, TX). Dichloromethane, toluene, and ϵ -caprolactone (ϵ -CL) were purchased from Sigma-Aldrich (Oakville, ON), dried under calcium hydride, and distilled prior to use. ¹¹¹InCl₃ was purchased from MDS Nordion (Kanata, ON). Synthetic 13-mer NLS peptides (CGYGPKKKRKVG) were synthesized by the Advanced Protein Technology Centre (Hospital for Sick Children, Toronto, ON), and sulfo-succinimidyl-4-(*N*-maleimidomethyl)-cyclohexane-1-carboxylate (sulfo-SMCC) was purchased from Pierce (Rockford, IL). Trastuzumab (Herceptin; Hoffman-La Roche) was obtained from the Pharmacy Department at William Osler Health Sciences Centre (Brampton, ON).

Cell Culture. BT-474 and MDA-MB-231 human BC cells were purchased from the American Type Culture Collection (Manassas, VA). BT-474 cells were cultured in RPMI 1640 supplemented with 10% fetal bovine serum (FBS; Sigma-Aldrich) and 1% (v/v) penicillin/streptomycin. MDA-MB-231 cells were cultured in DMEM supplemented with 10% FBS and 1% (v/v) penicillin/streptomycin.

Synthesis and Characterization of Copolymer Materials. Copolymers including MePEG-*b*-PCL, COOH-PEG-*b*-PCL, and NH₂-PEG-*b*-PCL were prepared by cationic ring-opening polymerization of ϵ -CL as described elsewhere.^{29,34,35} *N*-Hydroxysuccinimide-PEG-*b*-PCL (NHS-PEG-*b*-PCL) copolymer was prepared by NHS activation of COOH-PEG-*b*-PCL in the presence of *N,N'*-Dicyclohexylcarbodiimide (DCC) using an established method.³⁶ Copolymer compositions were determined by ¹H NMR spectroscopy and GPC analysis as published previously.^{37,38}

For copolymer radiolabeling, DTPA-PEG-*b*-PCL was prepared using a method described in detail elsewhere³⁸ and chelated with the radionuclide ¹¹¹In. Briefly, a 2-fold molar excess of *p*-SCN-Bn-DTPA was reacted with NH₂-PEG-*b*-PCL. Excess *p*-SCN-Bn-DTPA was isolated and removed via size exclusion chromatography (Bio-Gel P2; BioRad, CA). Purified DTPA-PEG-*b*-PCL was lyophilized in aliquots. Immediately prior to experimental use, purified DTPA-PEG-*b*-PCL was incubated with ¹¹¹In for 30 min in 0.1 M sodium acetate buffer (pH = 6). Radiochemical purity was assessed using instant thin layer chromatography (ITLC) and found to exceed 96%, as described previously.³⁸

Copolymer bearing NLS and trastuzumab Fab (NLS-TmAb-Fab-PEG-*b*-PCL) was prepared and characterized as described elsewhere.²⁹ Briefly, a 15-fold molar excess of sulfo-SMCC was reacted with TmAb-Fab for 1 h at room temperature (RT). This ratio of sulfo-SMCC to TmAb-Fab was found to result in two NLS peptides bound per TmAb-Fab antibody as previously published.²⁹ Unbound sulfo-SMCC was removed by running the mixture through a Sephadex-G50 minicolumn eluted 30 times with 100 μ L aliquots of phosphate-buffered saline (PBS, pH 7.4). The maleimide-derivatized TmAb-Fab was concentrated using a Microcon YM-50 ultrafiltration device (Amicon) and subsequently reacted with a 60-fold molar excess of NLS peptides (5–10 mmol/L in PBS, pH 7.4) overnight at 4 °C.

Purification was achieved using a Sephadex-G50 minicolumn to remove unbound NLS. The NLS-TmAb-Fab was reacted with a 5-fold molar excess of NHS-PEG-*b*-PCL and purified by SEC on a Bio-Gel P-30 column with PBS (pH 7.4) as the eluent. This had previously been shown to result in a 1:1 (copolymer–antibody) ratio.²⁹ The purity and homogeneity of NLS-TmAb-Fab and NLS-TmAb-Fab-PEG-*b*-PCL were assessed by sodium dodecyl sulfate polyacrylamide gel electrophoresis (SDS-PAGE) developed on a 4–20% Tris-HCl gradient minigel and stained with Coomassie brilliant blue R-250. Radiolabeling TmAb-Fab-NLS₂ with ¹¹¹In was achieved using an established method.^{29,39}

Preparation and Characterization of BCMs. MePEG-*b*-PCL copolymer was dissolved in DMF for 4 h with continuous stirring and dried under nitrogen to form a dry copolymer film. The film was left under vacuum overnight at RT to remove residual solvent. Subsequently, the film was hydrated with a 1 mL aliquot of PBS (pH 7.4, 0.01 M) at 60 °C to form BCMs at a copolymer concentration of 50 mg/mL. Radiolabeled ¹¹¹In-PEG-*b*-PCL copolymers were incorporated into the preformed BCMs via the transfer method³⁶ to form nontargeted ¹¹¹In-BCMs. Briefly, ¹¹¹In-PEG-*b*-PCL (<2 mol %) were added to the preformed BCMs for 1 h at 60 °C and left to stir overnight at RT to promote uniform distribution of the radiolabeled copolymers within the preformed BCMs. Similarly, NLS₂-TmAb-Fab-PEG-*b*-PCL (<2 mol %) or TmAb-Fab-PEG-*b*-PCL (no NLS) were incorporated into the preformed BCMs to form ¹¹¹In/NLS₂-TmAb-Fab-BCMs and ¹¹¹In/TmAb-Fab-BCMs, respectively.

The hydrodynamic diameter and zeta potential of the BCMs were determined by dynamic light scattering (DLS) using a 90 Plus Particle Size Analyzer (Brookhaven Instruments Corp., NY). The morphology of the micelles was evaluated by transmission electron microscopy (TEM) with a Hitachi 7000 microscope operating at an acceleration voltage of 75 kV (Schaumburg, IL).

Tumor Inoculation. Female athymic CD-1 mice (Charles River, Wilmington, MA), 4–5 weeks of age, were first implanted subcutaneously with a 0.72 mg, 60-day sustained-release 17 β -estradiol pellet (Innovative Research, Sarasota, FL). One day after implantation of the 17 β -estradiol pellet, 1.0×10^7 BT-474 or 1×10^6 MDA-MB-231 cells in 100 μ L of culture medium and Matrigel (BD Biosciences, Mississauga, ON) (1:1 vol/vol) were injected subcutaneously in the right hind limb. Two-to-four weeks postinoculation, mice bearing 50–100 mm³ tumors were selected for *in vivo* testing ($n = 3$ –5 mice per group). Animal studies were conducted under a protocol approved by the Animal Care Committee at the University Health Network and followed Canadian Council on Animal Care guidelines.

Evaluation of Pharmacokinetics and Biodistribution. The pharmacokinetics of ¹¹¹In/NLS₂-TmAb-Fab-BCMs was evaluated in athymic mice bearing subcutaneous BT-474 (1 – 2×10^6 HER2 receptors/cell) or MDA-MB-231 (0.5×10^5 HER2 receptors/cell) human BC tumor xenografts. Mice bearing 50–100 mm³ tumors ($n = 3$ –5 mice/group) were intravenously injected with 4.0–6.8 mCi/kg (250 mg of copolymer/kg) of ¹¹¹In/NLS₂-TmAb-Fab-BCMs. Controls included mice receiving: (i) nontargeted ¹¹¹In-BCMs to evaluate the contribution of passive targeting alone (EPR effect) vs HER2 targeting for tumor localization, (ii) ¹¹¹In/TmAb-Fab-BCMs (no NLS) to investigate the effectiveness of NLS in facilitating nuclear translocation of the BCMs, and (iii)

¹¹¹In-TmAb-Fab-NLS₂ to assess the impact of BCM surface ligation on pharmacokinetics and biodistribution. Blood samples were collected at 0.083, 0.25, 0.5, 1, 2, 4, 8, 12, 24, and 48 h postinjection (p.i.) by saphenous vein puncture into heparinized microcapillary tubes. The volume of blood collected was measured, and the radioactivity was counted in a γ -counter. The blood concentration of ¹¹¹In was expressed as % injected dose per milliliter (% i.d./mL) and plotted against time postinjection. At 48 h p.i., the mice were anaesthetized and sacrificed by cardiac puncture. Major organs including the liver, spleen, heart, lungs, kidneys, and tumor were excised, weighed, and counted on a γ -counter. Uptake of radioactivity was expressed as mean \pm standard deviation (SD) percent injected dose per gram (% i.d./g) of organ. Tumor/normal tissue (T/NT) ratios were calculated as a metric of tumor targeting ability. Scientist v.2.01 software (MicroMath Scientific Software, St. Louis, MO) was used to fit the pharmacokinetic data, using least-squares fitting parameters based upon a two-compartment model.

MicroSPECT/CT Imaging. Tumor-bearing mice were intravenously injected with 50 mCi/kg of ¹¹¹In/NLS₂-TmAb-Fab-BCMs (250 mg copolymer/kg) or ¹¹¹In-TmAb-Fab-NLS₂ (5 mg/kg). Single photon emission computed tomography (SPECT) enabled the acquisition of highly resolved and sensitive images using a microSPECT/CT small animal tomograph (Bioscan NanoSPECT) at 24 and 48 h p.i. Cone-beam CT scans (180 projections, 1 s/projection, 45 kVp, 0.18 mA) were performed prior to helical SPECT image acquisition for anatomical reference. Co-registration of SPECT and CT images was performed using InvivoScope software (Bioscan). Region of interest (ROI) analysis of the transverse tumor slices revealed qualitative information on the distribution and tumor penetration of the ¹¹¹In/NLS₂-TmAb-Fab-BCMs or ¹¹¹In-TmAb-Fab-NLS₂ within the tumor tissue.

Fluorescence Microscopy and Image Analysis. Immediately following microSPECT/CT imaging at 48 h p.i., mice were intravenously injected with a solution of bisbenzamide Hoechst 33342 (40 mg/kg, Sigma-Aldrich), anaesthetized, and sacrificed by cervical dislocation 30–60 s postinjection. Tumors were promptly excised, embedded in Tissue-Tek OCT compound (Sakura Finetek, Alphen aan den Rijn, NL), and frozen in liquid nitrogen. Tumor blocks were stored at –80 °C prior to undergoing cryosectioning and staining (Pathology Research Program, University Health Network). Three serial 8 μ m-thick sections were cut, and whole tumor sections were viewed under an upright Olympus BX50 fluorescence microscope (Olympus, PA) equipped with a motorized stage for whole-slide imaging. Unstained tumor sections were first imaged for Hoechst signal ($\lambda_{\text{ex}}/\lambda_{\text{em}} = 350/461$ nm), providing visualization of perfused microvessels within the tumor. These same sections were subsequently stained for the endothelial cell marker, CD31, using primary hamster anti-CD31 (Chemicon) and secondary Cy2-conjugated goat antihamster IgG ($\lambda_{\text{ex}}/\lambda_{\text{em}} = 492/510$ nm; Jackson ImmunoResearch, West Grove, PA) antibodies and reimaged for visualization of total (perfused and nonperfused) blood vessels within the tumor. Whole tumor images were generated by stitching individually acquired tiles together using ImagePro PLUS software (Media Cybernetics, Rockville, MD) and employed as such. Prior to analysis, whole tumor images underwent preprocessing to exclude artifacts using Fiji image processing package.⁴⁰ The region of interest (i.e., whole tumor) was isolated by generating a tumor mask and eliminating nontumor tissue in ImagePro PLUS.

Composite images depicting both Hoechst and CD31 signal were also generated.

Microvessel density (MVD) was evaluated using a customized image analysis algorithm in MATLAB (v.7.5.0.342, R2007b). 16-bit grayscale whole tumor blood vessel images were thresholded to identify CD31- or Hoechst-stained blood vessel structures relative to background (e.g., tumor tissue). The images were subsequently binarized and positive pixel areas determined. In particular, the total vessel area was computed as the ratio of CD31-positive area to total tumor area. Similarly, the total perfused area was determined as the ratio of Hoechst-positive area to total tumor area. In addition, a third parameter was determined to compensate for the diffusion of Hoechst from perfused vessels and the resulting area overestimate. Accordingly, the intersecting area of both Hoechst- and CD31-positive pixels was divided by total tumor area to yield the third characteristic ratio (i.e., corrected perfused vessel area).

Autoradiography. Building upon previously published work,³⁷ autoradiographic imaging was used to provide further insight into the intratumoral distribution of ¹¹¹In/NLS₂-TmAb-Fab-BCMs relative to ¹¹¹In-TmAb-Fab-NLS₂ in the high HER2 expressing BT-474 model. Superimposition of the autoradiographic images with highly resolved fluorescence images depicting tumor vasculature enables correlation between BCM tumor microdistribution and the underlying regional MVD. Autoradiographic imaging was conducted following an established method.⁴¹ Briefly, 7–10 days following tumor excision, unstained tumor sections were exposed to a MultiSensitive screen (PerkinElmer, MA) for 24–96 h. The film was loaded into the Cyclone Plus Storage Phosphor System (PerkinElmer, MA), and the autoradiographic image was recorded. This image was overlaid with its corresponding fluorescence image (consecutively sectioned) using Adobe Photoshop CS4 (v.11.0) and arbitrarily subdivided into 0.5 × 0.5 mm² sections. The radioactivity in each 0.5 × 0.5 mm² area was quantified using the OptiQuant Image Analysis software (PerkinElmer, MA) and expressed as digital light units (DLU). The MVD in each 0.5 × 0.5 mm² area in the corresponding fluorescence image was determined by a custom user-generated MATLAB algorithm. Pearson correlation and linear regression analyses were used to investigate the relationship between ¹¹¹In uptake (i.e., DLU) and MVD in each 0.5 × 0.5 mm² section.

In Vivo Subcellular Fractionation. Tumors harvested at 48 h p.i. from biodistribution studies were fractionated using a validated method detailed elsewhere.^{41,42} Briefly, tumors were minced, suspended in an acidic sodium acetate buffer (pH 2.5), homogenized using a Sonic Dismembrator-model 100 (Fisher Scientific, Pittsburgh, PA), and incubated on ice for 10 min. The extracellular and membrane-bound radioactivity displaced following the acidic wash was isolated by centrifugation at 6311 × g for 10 min. Following a PBS rinse, the cells were homogenized in Nuclei PURE Prep lysis buffer (Nuclei PURE Prep Nuclei Isolation Kit; Sigma-Aldrich). The nuclei were isolated from the cytoplasm via ultracentrifugation through a sucrose cushion solution. The cell pellet containing the nuclear fraction, as well as the corresponding supernatant containing the cytoplasm, extracellular, and membrane-bound fractions were counted in a γ-counter.

Statistical Analysis. All results were obtained in triplicate and reported as the mean ± SD. Statistical analysis was conducted using SPSS (Statistical Package for the Social Sciences, v. 14.0). One-way parametric analysis of variance

(ANOVA) with the Bonferroni correction for multiple comparisons was used to compare three or more groups if the ANOVA *F*-test indicated a statistical significance. All other statistical comparisons were made using the Student's *t*-test with *p* < 0.05 considered a statistical significance. Pearson correlation and linear regression were used to evaluate the autoradiography data.

RESULTS

Physicochemical Characterization of Copolymers and Micelles. As previously published,²⁹ physicochemical characterization of polymer materials using ¹H NMR, GPC, and SDS-PAGE analyses revealed successful synthesis of NLS₂-NHS-PEG-*b*-PCL and ¹¹¹In-DTPA-PEG-*b*-PCL with a narrow molecular weight distribution and high radiochemical purity. The micelles were shown to be ~31 nm in diameter, as estimated using dynamic light scattering, with a zeta potential of -2.1 ± 2.4 mV.²⁹ Evaluation of the morphology of ¹¹¹In/NLS₂-TmAb-Fab-BCMs at a concentration of 50 mg/mL by TEM revealed a homogeneous population of spherical aggregates.²⁹

Evaluation of Pharmacokinetics and Biodistribution.

Figure 1 presents the concentration of radioactivity in the blood of mice bearing BT-474 (Figure 1A) or MDA-MB-231 (Figure 1B) tumors and injected intravenously with ¹¹¹In/NLS₂-TmAb-Fab-BCMs, ¹¹¹In/TmAb-Fab-BCMs (no NLS), ¹¹¹In-BCMs, and ¹¹¹In-TmAb-Fab-NLS₂, at selected time points up to 48 h p.i.

The data were fit using a two-compartment pharmacokinetic model. Estimated values of the pharmacokinetic parameters are summarized in Table 1. All four formulations were found to demonstrate a biphasic elimination profile characterized by a rapid distribution phase and a prolonged elimination phase. Pharmacokinetic parameters for all three BCM formulations did not differ significantly across both tumor models.

The β-phase half-life was significantly longer for the ¹¹¹In/NLS₂-TmAb-Fab-BCMs in comparison to ¹¹¹In-TmAb-Fab-NLS₂ in both tumor xenograft models (*t*_{1/2,β} = 22.8 ± 5.07 vs 12.6 ± 3.28 h and 20.6 ± 4.87 vs 8.27 ± 1.96 h, in the BT-474 and MDA-MB-231 tumor xenograft-bearing mice, *p* = 0.043 and *p* = 0.008, respectively).

The area under the blood concentration versus time curve value for the ¹¹¹In/NLS₂-TmAb-Fab-BCMs (AUC = 1547 ± 145% i.d. h/mL) was approximately 2-fold higher than that for ¹¹¹In-TmAb-Fab-NLS₂ (AUC = 868 ± 466% i.d. h/mL) in BT-474 tumor-bearing mice. A similar trend was observed in MDA-MB-231 tumor-bearing mice. This indicates that formulations relying on BCMs were eliminated more slowly from the blood than ¹¹¹In-TmAb-Fab-NLS₂. In mice bearing BT-474 tumor xenografts, the volume of distribution of the central compartment (*V*₁) for ¹¹¹In/NLS₂-TmAb-Fab-BCMs was comparable to ¹¹¹In-TmAb-Fab-NLS₂ (*p* = 1). Similarly, the volume of distribution at “steady-state” (*V*_{ss}) was comparable between ¹¹¹In/NLS₂-TmAb-Fab-BCMs and ¹¹¹In-TmAb-Fab-NLS₂ (*p* = 1). These trends were also observed in the MDA-MB-231 tumor model. Taken together, these results suggest that the BCMs and ¹¹¹In-TmAb-Fab-NLS₂ are confined to the blood volume.

Figure 2 includes the tumor (T) and normal tissue (NT) uptake of ¹¹¹In/NLS₂-TmAb-Fab-BCMs, ¹¹¹In/TmAb-Fab-BCMs (no NLS), ¹¹¹In-BCMs, and ¹¹¹In-TmAb-Fab-NLS₂ at 48 h p.i. in athymic mice bearing subcutaneous BT-474 (Figure

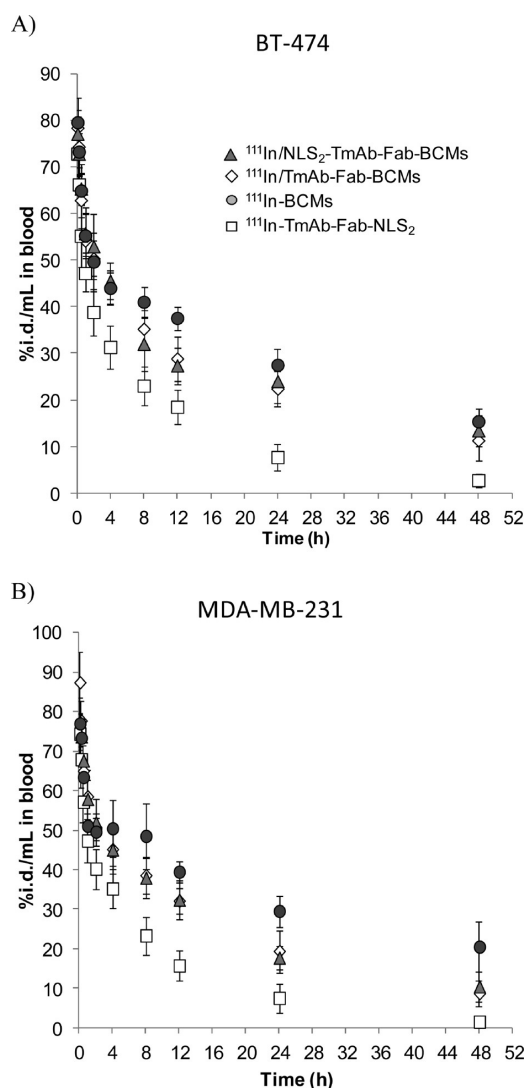


Figure 1. Percent injected dose of radioactivity remaining in the blood per milliliter at various time points postinjection of $^{111}\text{In}/\text{NLS}_2\text{-TmAb-Fab-BCMs}$, $^{111}\text{In}/\text{TmAb-Fab-BCMs}$ (no NLS), $^{111}\text{In-BCMs}$, and $^{111}\text{In-TmAb-Fab-NLS}_2$ in mice bearing (A) BT-474 or (B) MDA-MB-231 xenografts.

2A) or MDA-MB-231 (Figure 2B) xenografts. Similarly, T/NT ratios are presented in Table 2.

$^{111}\text{In}/\text{NLS}_2\text{-TmAb-Fab-BCMs}$ demonstrated specific HER2-mediated uptake in BT-474 tumors. In fact, all three formulations relying on HER2 targeting using TmAb-Fab

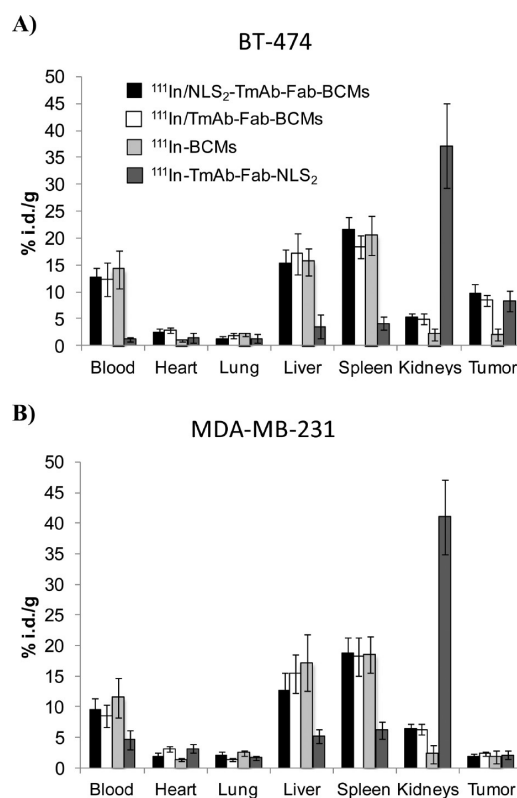


Figure 2. Tumor and normal tissue uptake of $^{111}\text{In}/\text{NLS}_2\text{-TmAb-Fab-BCMs}$, $^{111}\text{In}/\text{TmAb-Fab-BCMs}$ (no NLS), $^{111}\text{In-BCMs}$, and $^{111}\text{In-TmAb-Fab-NLS}_2$ at 48 h p.i. in athymic mice bearing (A) BT-474 or (B) MDA-MB-231 xenografts.

exhibited both higher tumor uptake (Figure 2) and tumor-to-blood ratios, relative to nontargeted $^{111}\text{In-BCMs}$ in the high HER2-expressing BT-474 cells (Table 2). The greater levels of tumor uptake and tumor-to-blood ratios of $^{111}\text{In}/\text{NLS}_2\text{-TmAb-Fab-BCMs}$, $^{111}\text{In}/\text{TmAb-Fab-BCMs}$, and $^{111}\text{In-TmAb-Fab-NLS}_2$ contrast significantly with the lower levels achieved in the low HER2-expressing MDA-MB-231 model ($p < 0.01$).

Tumor uptake of $^{111}\text{In}/\text{NLS}_2\text{-TmAb-Fab-BCMs}$ was approximately 5-fold greater in BT-474 xenografts relative to MDA-MB-231 xenografts (% i.d./g = 9.73 ± 1.68 vs 1.89 ± 0.36 , $p = 0.001$). Similarly, tumor uptake of $^{111}\text{In}/\text{TmAb-Fab-BCMs}$ and $^{111}\text{In-TmAb-Fab-NLS}_2$ was 4-fold higher in BT-474 relative to MDA-MB-231 tumors (% i.d./g = 8.44 ± 1.08 vs 2.33 ± 0.31 and 8.30 ± 1.66 vs 2.08 ± 0.72 , $p = 0.001$ and 0.004 , respectively). Formulations relying on BCMs accumulated

Table 1. Summary of Pharmacokinetic Parameters^a

	sample	$t_{1/2,\alpha}$ (h)	$t_{1/2,\beta}$ (h)	V_1 (mL)	V_{ss} (mL)	CL (mL/h)	AUC (%i.d. h/mL)
BT-474	$^{111}\text{In}/\text{NLS}_2\text{-TmAb-Fab-BCMs}$	0.82 ± 0.32	22.8 ± 5.07	1.3 ± 0.11	2.06 ± 0.33	0.07 ± 0.01	1547 ± 145
	$^{111}\text{In}/\text{TmAb-Fab-BCMs}$	0.51 ± 0.20	20.7 ± 5.21	1.2 ± 0.02	2.00 ± 0.05	0.07 ± 0.02	1478 ± 401
	$^{111}\text{In-BCMs}$	0.43 ± 0.12	24.2 ± 1.95	1.2 ± 0.06	1.90 ± 0.15	0.06 ± 0.00	1826 ± 154
	$^{111}\text{In-TmAb-Fab-NLS}_2$	0.49 ± 0.08	12.6 ± 3.28	1.3 ± 0.06	2.06 ± 0.07	0.14 ± 0.07	868 ± 466
MDA-MB-231	$^{111}\text{In}/\text{NLS}_2\text{-TmAb-Fab-BCMs}$	0.70 ± 0.28	20.6 ± 4.87	1.2 ± 0.07	1.93 ± 0.19	0.07 ± 0.02	1517 ± 339
	$^{111}\text{In}/\text{TmAb-Fab-BCMs}$	0.53 ± 0.55	21.2 ± 1.19	1.0 ± 0.16	1.91 ± 0.24	0.06 ± 0.01	1577 ± 176
	$^{111}\text{In-BCMs}$	0.36 ± 0.06	25.1 ± 2.26	1.2 ± 0.09	1.89 ± 0.09	0.05 ± 0.01	1911 ± 269
	$^{111}\text{In-TmAb-Fab-NLS}_2$	0.37 ± 0.13	8.27 ± 1.96	1.2 ± 0.10	2.04 ± 0.30	0.18 ± 0.03	568 ± 96

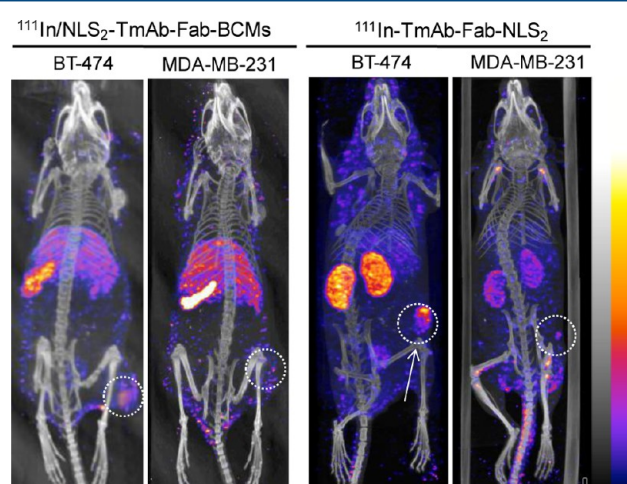
^a $t_{1/2,\alpha}$ = alpha half-life, $t_{1/2,\beta}$ = beta half-life, V_1 = volume of distribution, V_{ss} = volume of distribution at steady-state, CL = clearance rate, AUC = area under the curve.

Table 2. Uptake of ^{111}In -Labeled BCMs vs ^{111}In -TmAb-Fab-NLS₂ at 48 h p.i., Expressed as Tumor-to-Normal Tissue Ratios

tissue	$^{111}\text{In}/\text{NLS}_2\text{-TmAb-Fab-BCMs}$	$^{111}\text{In}/\text{TmAb-Fab-BCMs}$	$^{111}\text{In-BCMs}$	$^{111}\text{In-TmAb-Fab-NLS}_2$
BT-474				
blood	0.73 ± 0.09	0.65 ± 0.06	0.14 ± 0.01	7.41 ± 0.63
heart	3.63 ± 0.58	2.71 ± 0.43	1.89 ± 0.33	5.87 ± 0.55
lung	8.01 ± 0.63	4.74 ± 0.81	0.92 ± 0.13	6.11 ± 0.61
liver	0.62 ± 0.05	0.46 ± 0.05	0.13 ± 0.02	2.31 ± 0.45
spleen	0.42 ± 0.07	0.43 ± 0.05	0.10 ± 0.02	2.02 ± 0.47
kidneys	1.76 ± 0.22	1.60 ± 0.31	1.04 ± 0.13	0.22 ± 0.02
MDA-MB-231				
blood	0.18 ± 0.01	0.26 ± 0.04	0.15 ± 0.01	0.45 ± 0.11
heart	0.91 ± 0.13	0.72 ± 0.11	1.34 ± 0.41	0.63 ± 0.15
lung	0.89 ± 0.19	1.62 ± 0.16	0.76 ± 0.10	1.21 ± 0.30
liver	0.14 ± 0.02	0.14 ± 0.02	0.10 ± 0.01	0.40 ± 0.09
spleen	0.10 ± 0.01	0.12 ± 0.01	0.10 ± 0.02	0.34 ± 0.12
kidneys	0.28 ± 0.03	0.36 ± 0.06	0.81 ± 0.08	0.00 ± 0.00

mainly in the spleen and liver in comparison to ^{111}In -TmAb-Fab-NLS₂. For example, a 5-fold increase in liver and spleen uptake was observed for $^{111}\text{In}/\text{NLS}_2\text{-TmAb-Fab-BCMs}$ in comparison to ^{111}In -TmAb-Fab-NLS₂ in BT-474 tumor-bearing mice, while a 3-fold increase was noted in MDA-MB-231 tumor-bearing mice. This level of accumulation can be attributed to clearance of the BCMs via the MPS, a common elimination pathway for nanoparticles.^{43–47} In contrast, the ^{111}In -TmAb-Fab-NLS₂ formulation was shown to localize predominantly within the kidneys in comparison to the BCM formulations (i.e., % i.d./g = 37.2 ± 7.81 vs 5.37 ± 0.58 for $^{111}\text{In}/\text{NLS}_2\text{-TmAb-Fab-BCMs}$ in BT-474 tumor-bearing mice, for example; $p = 0.002$), due to the known high renal clearance of TmAb-Fab fragments.⁴⁸ This is evidenced by the very low tumor-to-kidney ratio observed for ^{111}In -TmAb-Fab-NLS₂ in both BT-474 and MDA-MB-231 tumor-bearing mice (0.22 ± 0.02 and 0.001 ± 0.000 , respectively). The tumor-to-blood ratio was significantly higher for the ^{111}In -TmAb-Fab-NLS₂ relative to the BCMs in both models owing to the faster elimination of ^{111}In -TmAb-Fab-NLS₂ from the blood circulation ($p < 0.05$). This finding indeed correlates with the pharmacokinetic profiles represented in Figure 1. Localization of ^{111}In -BCM in other normal tissues was assumed to be nonspecific and a result of blood pool radioactivity.

Assessment of Normal Tissue Uptake, Tumor Deposition and Intratumoral Distribution Using Noninvasive MicroSPECT/CT Imaging. As presented in Figure 3, normal tissue accumulation evaluated by microSPECT imaging corresponded well with results obtained in the conventional biodistribution studies (Figure 2). Expectedly, mice administered ^{111}In -TmAb-Fab-NLS₂ demonstrated significant kidney uptake in both the BT-474 and MDA-MB-231 tumor models in comparison to any of the formulations relying on BCMs ($p < 0.01$). In addition, significantly more ^{111}In -TmAb-Fab-NLS₂ was shown to be localized within BT-474 tumors relative to MDA-MB-231 tumors ($p = 0.008$). Specifically, ROI analysis of total tumor uptake revealed an approximately 5-fold greater accumulation of ^{111}In -TmAb-Fab-NLS₂ in the BT-474 tumors compared to the MDA-MB-231 tumors (9.58 ± 1.35 vs $2.16 \pm 0.42\%$ i.d./g, $p = 0.001$, respectively). Similarly, in mice administered $^{111}\text{In}/\text{NLS}_2\text{-TmAb-Fab-BCMs}$, BT-474 tumors exhibited a 4-fold higher concentration of radioactivity according to ROI analysis (8.59 ± 1.48 vs $2.39 \pm 0.71\%$ i.d./g, $p = 0.003$, respectively). As observed from the biodistribution

**Figure 3.** MicroSPECT/CT maximum intensity projection (MIP) of athymic mice bearing BT-474 or MDA-MB-231 xenografts acquired 48 h p.i. of $^{111}\text{In}/\text{NLS}_2\text{-TmAb-Fab-BCMs}$ or ^{111}In -TmAb-Fab-NLS₂. The white arrow points to the tumor.

studies, there was prominent uptake of $^{111}\text{In}/\text{NLS}_2\text{-TmAb-Fab-BCMs}$ in the liver and spleen in both tumor models.

A detailed examination of the tumor radioactivity at 48 h p.i. within transverse slices revealed a heterogeneous distribution of $^{111}\text{In}/\text{NLS}_2\text{-TmAb-Fab-BCMs}$ within the tumor mass, with a more pronounced localization of the NPs at the periphery (Figure 4A). Comparatively, ^{111}In -TmAb-Fab-NLS₂ was more evenly distributed throughout the tumor (Figure 4B). However, signal scattering and high background radioactivity due to the prolonged circulation half-life of $^{111}\text{In}/\text{NLS}_2\text{-TmAb-Fab-BCMs}$ and ^{111}In -TmAb-Fab-NLS₂ resulted in diminished spatial resolution (~ 0.8 mm). Thus, it was not possible to accurately assess the distribution of the radiolabeled micelles and antibody fragments at the microscopic level.

Fluorescence Microscopy. Widefield fluorescence microscopy was used to evaluate the degree of vascularization of the BT-474 and MDA-MB-231 tumor models. Fluorescence imaging of tumor microvessels provided insight into the number of microvessels per tumor area, as well as the functional status of those vessels in terms of perfusion (at 48 h p.i.). As illustrated in Figure 5, BT-474 tumors (A and B) appear less well-vascularized and perfused relative to MDA-MB-231 tumors (C and D). Table 3 summarizes MVD parameters

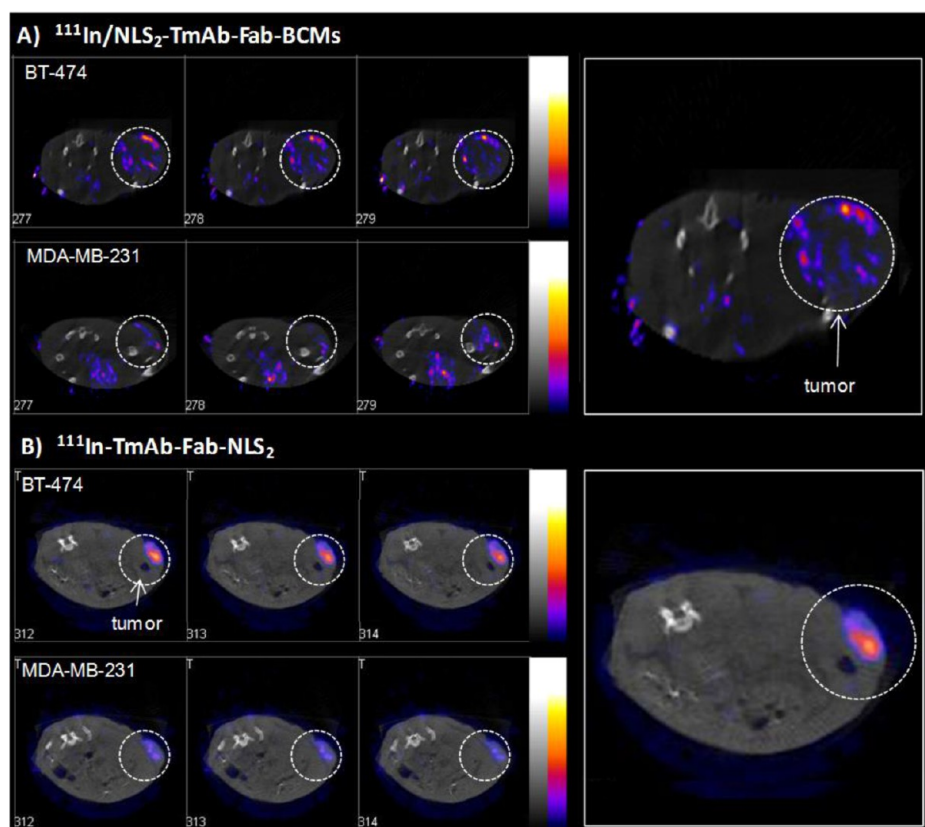


Figure 4. Three consecutive transverse slices of BT-474 or MDA-MB-231 tumors acquired after i.v. administration of (A) $^{111}\text{In}/\text{NLS}_2\text{-TmAb-Fab-BCMs}$ or (B) $^{111}\text{In-TmAb-Fab-NLS}_2$ at 48 h p.i.

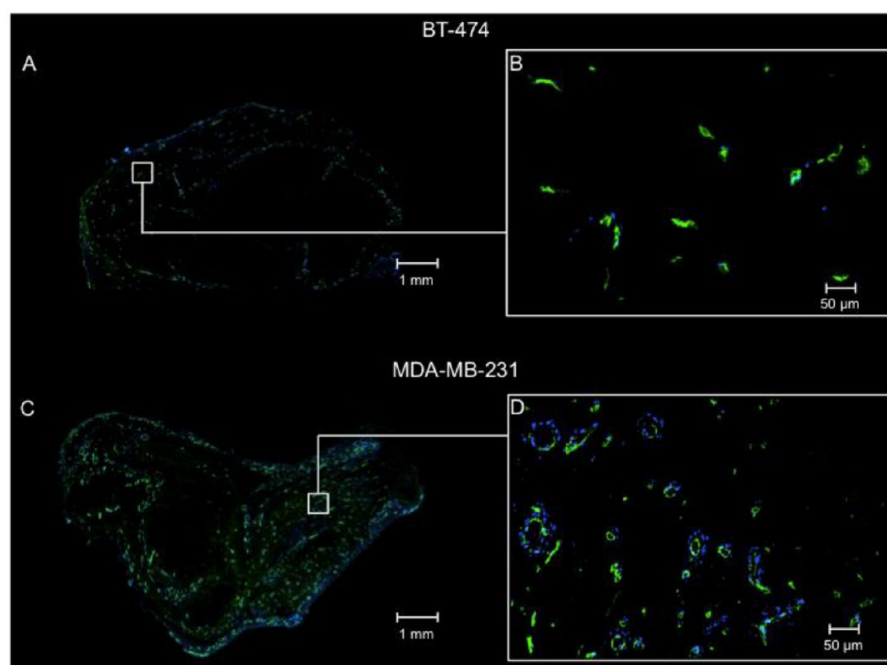


Figure 5. Composite images of perfused tumor vessels (Hoechst 33342, blue) and total vessels (green) in BT-474 (A and B) and MDA-MB-231 (C and D) tumor sections. B and D are 120 \times magnification.

determined to characterize the degree of vascularization in both models. In effect, BT-474 tumors were found to have an MVD of total microvessels (i.e., “total vessel area”) that was approximately 2-fold lower than in MDA-MB-231 tumors ($p = 0.004$). The MVD resulting from overlapping CD31 and

Hoechst signals (i.e., “corrected perfused vessel area”) was also found to be significantly lower in BT-474 relative to MDA-MB-231 tumors ($p = 0.025$), although MVD resulting from the perfusion signal alone was not found to differ significantly between both tumor models ($p = 0.069$). The latter MVD

Table 3. Microvessel Density in BT-474 ($n = 8$) and MDA-MB-231 ($n = 8$) Tumor Xenografts

MVD: total tumor area ^a	BT-174	MDA-MB-231
total perfused area	0.048 ± 0.021	0.094 ± 0.063
total vessel area	0.177 ± 0.095	0.419 ± 0.187
corrected perfused vessel area	0.036 ± 0.017	0.083 ± 0.050

^aRatio of microvessel density to total tumor area.

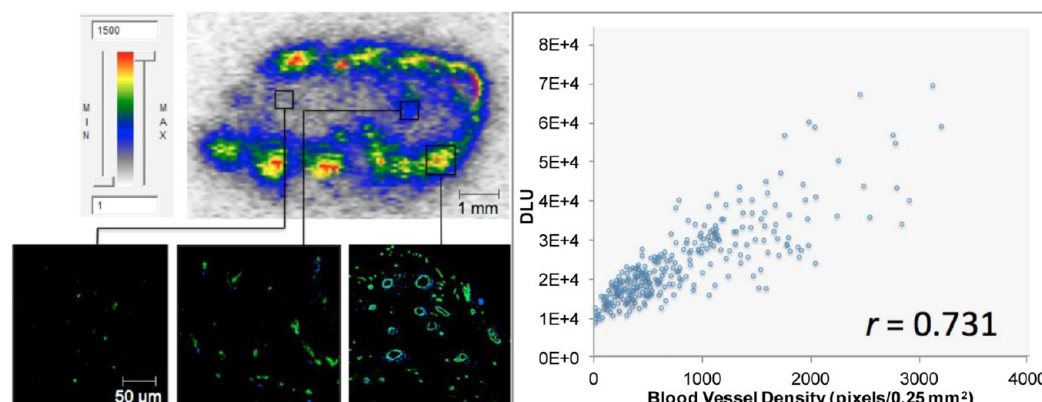
parameter (i.e., “total perfused area”) is considered to be an overestimate of tumor perfusion due to the greater degree of nuclear staining resulting from the diffusion of Hoechst dye into the extravascular space. Also, as shown in Figure 5, the BT-474 and MDA-MB-231 tumor sections include a large proportion of nonfunctional microvessels. Qualitatively, a greater number of microvessels was observed within the tumor periphery of both BT-474 and MDA-MB-231 tumors, with regions within the core of each tumor section exhibiting few or no microvessel structures.

Autoradiography. Intratumoral analysis of the distribution of ¹¹¹In/NLS₂-TmAb-Fab-BCMs (Figure 6A) and ¹¹¹In-TmAb-Fab-NLS₂ (Figure 6B) in BT-474 tumors using autoradiog-

raphy revealed a pattern of homogeneous uptake and distribution for the ¹¹¹In-TmAb-Fab-NLS₂ antibody fragments when compared to the radiolabeled BCMs, which were predominantly confined to the tumor periphery. This difference in tumor microdistribution between the radiolabeled NPs and the antibody fragments was similarly observed in MDA-MB-231 tumor xenografts (data not shown). This supports findings observed using the transverse projections of microSPECT/CT images (Figure 4). Similar to microSPECT/CT imaging, the resolution of autoradiography is limited by high background radioactivity, noise, and signal scattering, thereby effectively limiting this application to the evaluation of tissue distribution at the millimeter scale.

Pearson correlation analysis was used to evaluate the relationship between MVD and the distribution of radioactivity (i.e., ¹¹¹In) in specific regions of interest within the tumor sections. As presented in Table 4, the distribution of both ¹¹¹In/NLS₂-TmAb-Fab-BCMs and ¹¹¹In-TmAb-Fab-NLS₂ was positively correlated with MVD. This demonstrates that radiolabeled antibody fragments and NPs are localized primarily in regions of high MVD. Interestingly, the correlation between MVD and distribution of radioactivity (DLU)

A) ¹¹¹In/NLS₂-TmAb-Fab-BCMs



B) ¹¹¹In-TmAb-Fab-NLS₂

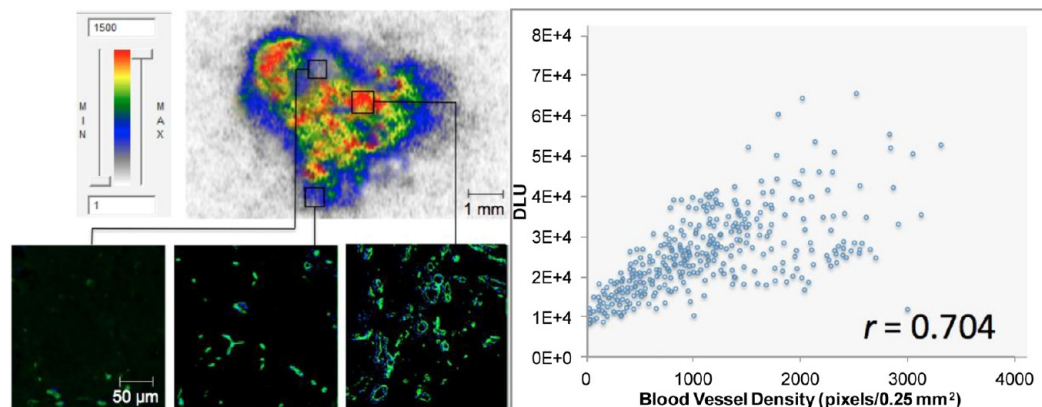


Figure 6. Microdistribution of (A) ¹¹¹In/NLS₂-TmAb-Fab-BCMs and (B) ¹¹¹In-TmAb-Fab-NLS₂ in BT-474 tumors. Tumor sections were imaged by autoradiography, followed by acquisition of fluorescence emitted by Hoechst-stained perfused vessels and, subsequently, CD31-stained tumor vessels. Autoradiographic images were coregistered with composite fluorescence images of the tumor vasculature. Pearson correlation and linear regression analyses were performed between the administered radioactivity and the inherent MVD of perfused tumor vessels (right).

Table 4. Pearson Correlation Coefficients for Radioactivity and MVD in BT-474 and MDA-MB-231 Tumor-Bearing Mice Administered ^{111}In -Labeled BCMs or ^{111}In -TmAb-Fab-NLS₂

		correlation coefficient (radioactivity vs MVD)		
		total perfused area	total vessel area	corrected area ^a
BT-474	$^{111}\text{In}/\text{NLS}_2\text{-TmAb-Fab-BCMs}$	0.683 ± 0.08	0.639 ± 0.12	0.714 ± 0.11
	$^{111}\text{In-TmAb-Fab-NLS}_2$	0.696 ± 0.06	0.627 ± 0.17	0.725 ± 0.09
MDA-MB-231	$^{111}\text{In}/\text{NLS}_2\text{-TmAb-Fab-BCMs}$	0.658 ± 0.13	0.631 ± 0.13	0.701 ± 0.07
	$^{111}\text{In-TmAb-Fab-NLS}_2$	0.689 ± 0.10	0.649 ± 0.11	0.725 ± 0.12

^aCorrected perfused vessel area (intersect of Hoechst and CD31 signals).

according to corrected perfused vessel area was strongest with an r^2 value of 0.714 ± 0.11 and 0.725 ± 0.09 for $^{111}\text{In}/\text{NLS}_2\text{-TmAb-Fab-BCMs}$ and $^{111}\text{In-TmAb-Fab-NLS}_2$ in BT-474 tumor sections, respectively. This was similarly observed in MDA-MB-231 tumor sections. Correlation coefficients for distribution of radioactivity and MVD as determined from total vessels (i.e., perfused and nonperfused) were lowest for both formulations in both tumor models.

In Vivo Subcellular Fractionation. Figure 7A and B illustrates the *in vivo* subcellular distribution of $^{111}\text{In}/\text{NLS}_2\text{-TmAb-Fab-BCMs}$.

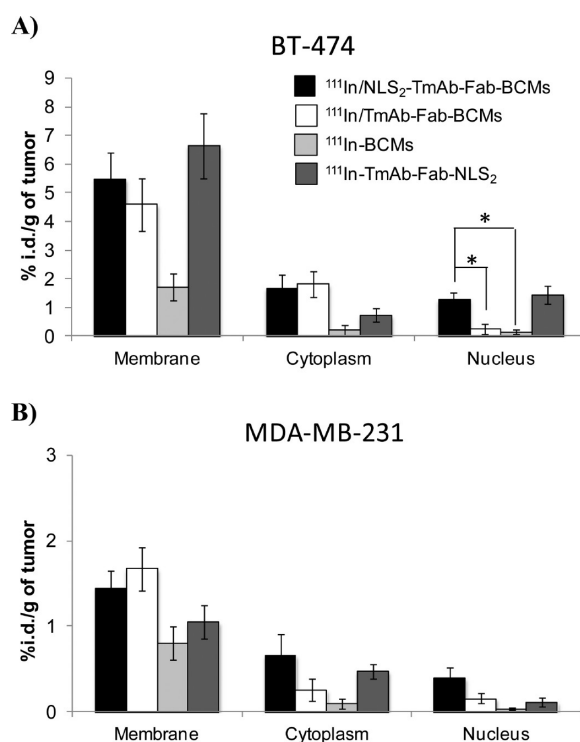


Figure 7. *In vivo* subcellular distribution of $^{111}\text{In}/\text{NLS}_2\text{-TmAb-Fab-BCMs}$, $^{111}\text{In}/\text{TmAb-Fab-BCMs}$ (no NLS), $^{111}\text{In-BCMs}$, and $^{111}\text{In-TmAb-Fab-NLS}_2$ in (A) BT-474 and (B) MDA-MB-231 tumor xenografts. Tumors were harvested at 48 h p.i. and disaggregated into extracellular, cytoplasmic, and nuclear fractions for which the radioactivity was determined using a γ -counter. * $p < 0.01$ as determined by independent t test.

TmAb-Fab-BCMs, $^{111}\text{In}/\text{TmAb-Fab-BCMs}$, $^{111}\text{In-BCMs}$, and $^{111}\text{In-TmAb-Fab-NLS}_2$ in BT-474 and MDA-MB-231 tumor-bearing mice, respectively, at 48 h p.i. The amount of $^{111}\text{In-BCMs}$ found within the extracellular (i.e., cell membrane-bound) and intracellular (i.e., cytoplasmic and nuclear) compartments was significantly lower than for the targeted formulations ($p < 0.01$) and comparable between BT-474 and

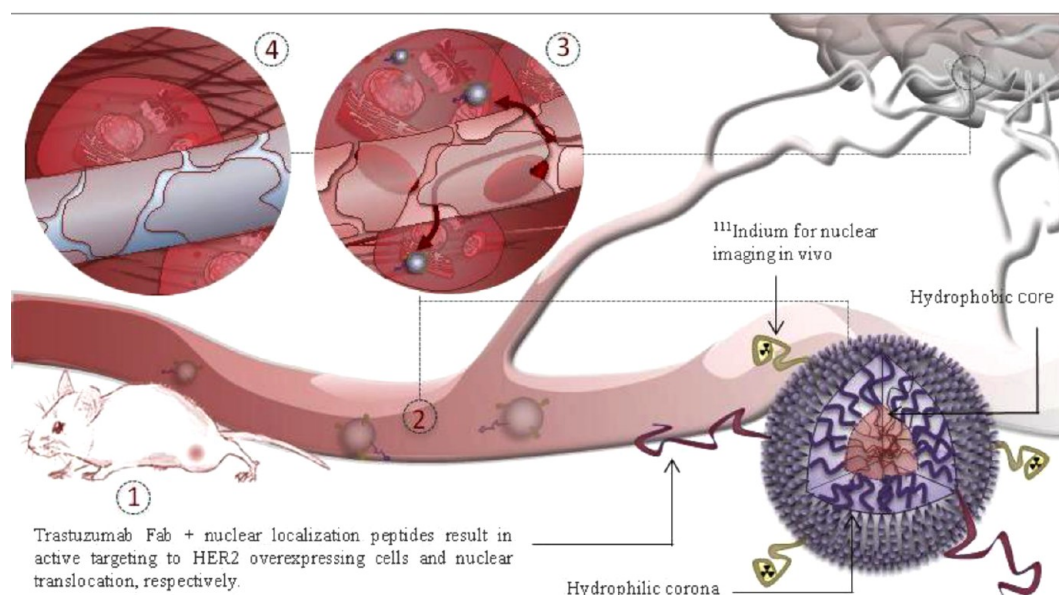
MDA-MB-231 tumors ($p > 0.05$). The uptake of the nontargeted BCMs can be attributed to nonspecific cellular association and internalization. Interestingly, cell membrane binding was comparable between $^{111}\text{In}/\text{NLS}_2\text{-TmAb-Fab-BCMs}$, $^{111}\text{In}/\text{TmAb-Fab-BCMs}$, and $^{111}\text{In-TmAb-Fab-NLS}_2$ in both tumor models (i.e., % i.d./g of tumor = 5.48 ± 0.92 vs 4.6 ± 0.95 vs 6.64 ± 1.12 in the BT-474 tumor model, respectively; $p > 0.05$).

Significant enhancement in cell association and uptake due to molecular targeting was found for the three targeted formulations in comparison to the nontargeted $^{111}\text{In-BCMs}$ in the BT-474 tumors expressing a higher level of HER2. Membrane-bound, cytoplasmic, and nuclear fractions of $^{111}\text{In}/\text{NLS}_2\text{-TmAb-Fab-BCMs}$ were approximately 3-fold higher in BT-474 tumors compared to MDA-MB-231 tumors. A 3-fold (membrane-bound), 7-fold (cytoplasmic), and 2-fold (nuclear) higher level of $^{111}\text{In}/\text{TmAb-Fab-BCMs}$ was found in BT-474 tumors relative to MDA-MB-231 tumors. $^{111}\text{In-TmAb-Fab-NLS}_2$ exhibited 6-fold higher membrane association and 12-fold higher nuclear uptake in BT-474 in comparison to MDA-MB-231 tumor cells. Interestingly, in the BT-474 cells, molecular targeting through conjugation of TmAb-Fab to BCMs resulted in significantly higher levels of cytoplasmic accumulation in comparison to $^{111}\text{In-TmAb-Fab-NLS}_2$ ($p < 0.05$) while the membrane-associated and nuclear levels of $^{111}\text{In}/\text{NLS}_2\text{-TmAb-Fab-BCMs}$ and $^{111}\text{In-TmAb-Fab-NLS}_2$ were comparable at 48 h p.i. ($p > 0.05$). A significant increase in the nuclear uptake of BCMs was observed between $^{111}\text{In}/\text{TmAb-Fab-BCMs}$ (no NLS) and $^{111}\text{In}/\text{NLS}_2\text{-TmAb-Fab-BCMs}$ in BT-474 tumors (% i.d./g of tumor = 0.252 ± 0.18 vs 1.28 ± 0.255 , respectively; $p = 0.005$). It should be noted that this difference in nuclear transport of TmAb-Fab-conjugated BCMs as a function of NLS functionalization was less prominent in MDA-MB-231 cells (% i.d./g of tumor = 0.155 ± 0.056 vs 0.398 ± 0.120 , respectively; $p = 0.503$).

DISCUSSION

Countless NP formulations have been designed to localize at solid tumor sites via exploitation of the EPR effect. Yet, a growing body of evidence suggests that total tumor accumulation of NPs is not the sole determinant of therapeutic efficacy. Specifically, studies have demonstrated that the intratumoral distribution, tumor penetration, and cellular localization of NPs have a significant impact on therapeutic outcomes.^{49–52} Studies of this kind highlight the importance of going beyond determination of bulk tumor accumulation of NPs to also examine distribution at the tissue, cellular, and subcellular levels.

At the whole body level, the main goal of any targeted NP system is to maximize accumulation at the target site while minimizing accumulation in nontarget organs or tissues. The

Scheme 1. The Fate of BCMs^a

^a(1) Mice bearing breast cancer tumor xenografts intravenously injected with ¹¹¹In/NLS₂-TmAb-Fab-BCMs. The radionuclide ¹¹¹In allows for non-invasive monitoring of the BCMs at the whole body level. (2) Non-ionic steric stabilizing PEG shell improves stability and prolongs circulation lifetime *in vivo*. (3) BCMs extravasate through leaky tumor vascular endothelium and are retained in the interstitium due to poor lymphatic drainage. TmAb-Fab binds to HER2 receptors. BCMs are taken up via receptor-mediated endocytosis and shuttled to the nucleus via interaction between cytoplasmic importins and NLS where Auger electrons emitted by ¹¹¹In are most damaging. (4) Regions of low microvessel density exhibit lower NP deposition.

current study examined the pharmacokinetics of various formulations and their biodistribution at 48 h postinjection in tumor xenograft models with low and high levels of HER2 expression. Previous studies have revealed that BCMs and TmAb-Fab attain maximum tumor accumulation at 48 h p.i.^{38,48} As shown in Figure 1, conjugation of the targeting moiety (NLS₂-TmAb-Fab) to the surface of the BCMs did not significantly alter their pharmacokinetic profile. The extended circulation lifetime of the nontargeted ¹¹¹In-BCMs enabled passive targeting to tumors (2–3% i.d./g) via the EPR effect (Scheme 1). Importantly, there was no significant difference in tumor accumulation of the nontargeted ¹¹¹In-BCMs between the MDA-MB-231 and BT-474 models despite the 2-fold higher perfused MVD (i.e., corrected perfused vessels) in the MDA-MB-231 model. These findings may highlight the spatial limitation associated with a two-dimensional assessment of tumor vasculature as well as the inherently dynamic nature of the vasculature.⁵³

The tumor accumulation of the actively targeted BCMs and the ¹¹¹In/NLS₂-TmAb-Fab is a result of both passive and active targeting. Interestingly, there was no significant difference in tumor accumulation between the actively targeted BCM formulations and ¹¹¹In/NLS₂-TmAb-Fab in either BT-474 or MDA-MB-231 models. The BT-474 cell line exhibits a 4- to 8-fold amplification of the HER2/neu gene, corresponding to a relative HER2 grade of 3+. HER2 densities are assessed using immunohistochemistry (IHC) staining and range from 0 to 3+. ^{54,55} The MDA-MB-231 cell line exhibits low levels of HER2 with a relative IHC-based HER2 grade of 0, which is comparable to normal mammary HER2/neu levels.⁵⁵ Effectively, the BT-474 and MDA-MB-231 tumor models selected in this study encompass both high and low degrees of HER2 expression, respectively. Here, a 5-fold increase in tumor accumulation was achieved upon conjugation of NLS₂-TmAb-

Fab to the BCMs in comparison to the nontargeted BCMs in the BT-474 model. In contrast, other recently published studies have shown that targeting of NPs to HER receptors (i.e., HER1 or EGFR, and HER2) via conjugation of ligands such as the epidermal growth factor (EGF) peptide and anti-HER2 monoclonal antibody fragments (Fab' or single chain Fv) to the surface of NPs does not result in an increase in tumor accumulation.^{17,41} Taken together, these findings emphasize that the influence of active targeting on bulk tumor accumulation is dependent on a range of variables; among them, the NP construct and ligand selected play a key role.

Although the evaluation of physicochemical characteristics, pharmacokinetics, and biodistribution of NPs such as BCMs has been explored extensively in the literature, only recently has the focus shifted to the evaluation of the spatial distribution of the NPs within whole tumor regions. Following extravasation from blood vessels, nanoparticles must penetrate the tumor interstitium to reach cancer cells.⁵⁶ The successful delivery and homogeneous distribution of NPs within tumors is particularly challenging due to the abnormal blood flow, dense nature of the extracellular matrix, and high interstitial fluid pressure.⁵⁷ Due to these biological barriers and previous findings in the literature, a NP size of approximately 31 nm was selected for the current study.⁴⁹ Reports have indicated that macromolecules of approximately 39 nm in diameter can be actively transported across the nuclear pore complex.⁵⁸ Yet, more recently, the transport of larger particles to the nucleus of cells using NLS has been reported. Misra et al. showed that doxorubicin (DOX)-loaded poly(D,L-lactide-co-glycolide) (PLGA) nanoparticles conjugated with NLS-FITC were able to enter the nuclei of human breast adenocarcinoma cells.⁵⁹ The NPs had a hydrodynamic diameter of 234 nm and exhibited 6-fold and 2-fold higher nuclear uptake than native DOX and unconjugated nanoparticles *in vitro*, respectively.⁵⁹

Moreover, Yu et al. have demonstrated successful nuclear targeting of NLS-conjugated cholesterol-modified glycol chitosan micelles with a hydrodynamic diameter of 248 nm.⁶⁰ However, in studies like these and others^{61,62} in which NPs with diameters much larger than the nuclear pore threshold have shown improved nuclear uptake, it remains unclear whether the uptake is associated with an active nuclear translocation mechanism or an alternate pathway. For example, it has been postulated that these NPs are able to enter the nucleus upon nuclear membrane collapse during cellular mitosis.⁶³

In the current study, fluorescence imaging of tumor microvessels was employed as a means to quantitatively characterize potential differences in the vasculature as a conduit for NP delivery. Detection of tumor microvessels by immunofluorescence was complemented by an indication of vascular perfusion at the time of animal sacrifice (i.e., 48 h p.i.). Such information allowed for the identification of relatively functional tumor vasculature in the assessment of MVD, for which the overlap between CD31 and Hoechst signals was employed to account for the considerable diffusivity of Hoechst away from blood vessels.⁶⁴ Autoradiography provided insight into the distribution of both ¹¹¹In-TmAb-Fab-NLS₂ and ¹¹¹In/NLS₂-TmAb-Fab-BCMs relative to the tumor vasculature. As mentioned previously, ¹¹¹In-TmAb-Fab-NLS₂ and ¹¹¹In/NLS₂-TmAb-Fab-BCMs were positively correlated with MVD, more so with our measure of perfused MVD (i.e., intersect of Hoechst 33342 and CD31 antibody). It is conceivable that the greater spatial correlation between the radioactive formulation and perfused vasculature is due to the ability of those vessels to deliver the systemically administered formulations; however further studies into the perfusion status of tumor vasculature throughout the course of the study are warranted in order to support this claim.

The incorporation of cell-specific ligands can modulate the distribution and retention of NPs in tumor cells. For example, Lee et al. have demonstrated that, although conjugation of targeting moieties to BCMS did not improve tumor uptake, it significantly increased the degree of cell association and internalization of the particles.⁴¹ While an important degree of NP accumulation at the tumor site can be attributed to the EPR effect, active targeting may enhance the retention of the vehicles within the tumor interstitium via cellular association and uptake. Importantly, an increase in the cellular internalization of a delivery system may lead to an increase in bioavailable drug. An improved understanding of the influence of active targeting on the biological fate of BCMS is necessary for their successful development as drug delivery formulations.

In the current study, *in vivo* cell fractionation of tumor tissue revealed significant increases in cell association and uptake of the actively targeted ¹¹¹In/NLS₂-TmAb-Fab-BCMs due to HER2 and nuclear targeting in BT-474 tumors. This work effectively supports the capability to promote greater tumor accumulation by functionalization of NPs with tumor-cell specific targeting moieties. Furthermore, we have shown that nuclear targeting through conjugation of NLS results in a significant increase in nuclear uptake. Thus, by exploiting the intrinsic nuclear translocation properties of NLS peptides, it is possible to effectively shuttle drug delivery systems such as BCMS to the nuclear and perinuclear regions of tumor cells *in vivo*. Nuclear localization of delivery vehicles is of particular interest given that there are a number of therapeutic agents with sites of action within this region. The use of ¹¹¹In as an

Auger electron emitter is supported by microdosimetry modeling, which has shown that the radiation dose absorbed within the cell nucleus is 35-fold greater relative to the extracellular decay of ¹¹¹In. Similarly, a modest 2-fold increase in radiation dose absorbed within the cytoplasm further corroborates the need for nuclear translocation of the radiolabeled nanosystem.⁶⁵

Here, we present an effective approach to targeting HER2-overexpressing tumors, leading to greater tumor accumulation and cellular uptake of BCMS via active targeting. Given the enhanced deposition of BCMS in the HER2-overexpressing BT-474 model relative to MDA-MB-231 tumors exhibiting low levels of HER2, these results strongly suggest that tumor expression of the targeted HER2 antigen plays a critical role in the effective accumulation and site-specific localization of HER2-targeted drug delivery systems *in vivo*.^{66,67} Further, the nuclear localization of the targeted nanosystem promises the efficient delivery of a number of therapeutics ranging from DNA-intercalating chemotherapeutic agents to genetic material. Future studies will entail an assessment of efficacy to verify whether the increased tumor accumulation and nuclear localization achieved through active targeting result in an improved therapeutic effect.

AUTHOR INFORMATION

Corresponding Author

*Leslie Dan Faculty of Pharmacy, University of Toronto, 144 College St., Toronto, Ontario, M5S 3M2, Canada. Phone: (416) 946-8594. Fax: (416) 978-8511. E-mail: cj.allen@utoronto.ca.

Author Contributions

[†]B.H. and S.N.E. contributed equally.

Notes

The authors declare no competing financial interest.

ACKNOWLEDGMENTS

The authors would like to acknowledge the Spatial-Temporal Targeting and Amplification of Radiation Response (STTARR) program and its affiliated funding agencies for providing the customized MATLAB algorithm used for image analysis. This study was supported by funding from the Ontario Institute for Cancer Research 1 mm Challenge Program, Canadian Breast Cancer Research Alliance and Canadian Institutes of Health Research to R.M.R. and C.A. An MDS-Nordion Graduate Scholarship in Radiopharmaceutical Sciences and an Ontario Graduate Scholarship were awarded to B.H. A CIHR Training Grant in Biological Therapeutics was awarded to S.N.E.

REFERENCES

- (1) Danson, S.; Ferry, D.; Alakhov, V.; Margison, J.; Kerr, D.; Jowle, D.; Brampton, M.; Halbert, G.; Ranson, M. Phase I dose escalation and pharmacokinetic study of pluronic polymer-bound doxorubicin (SP1049C) in patients with advanced cancer. *Br. J. Cancer* **2004**, *90*, 2085–91.
- (2) Kim, D. W.; Kim, S. Y.; Kim, H. K.; Kim, S. W.; Shin, S. W.; Kim, J. S.; Park, K.; Lee, M. Y.; Heo, D. S. Multicenter phase II trial of Genexol-PM, a novel Cremophor-free, polymeric micelle formulation of paclitaxel, with cisplatin in patients with advanced non-small-cell lung cancer. *Ann. Oncol.* **2007**, *18* (12), 2009–2014.
- (3) Matsumura, Y.; Hamaguchi, T.; Ura, T.; Muro, K.; Yamada, Y.; Shimada, Y.; Shirao, K.; Okusaka, T.; Ueno, H.; Ikeda, M.; Watanabe, N. Phase I clinical trial and pharmacokinetic evaluation of NK911, a micelle-encapsulated doxorubicin. *Br. J. Cancer* **2004**, *91*, 1775–81.

- (4) Hamaguchi, T.; Kato, K.; Yasui, H.; Morizane, C.; Ikeda, M.; Ueno, H.; Muro, K.; Yamada, Y.; Okusaka, T.; Shirao, K.; Shimada, Y.; Nakahama, H.; Matsumura, Y. A Phase I and pharmacokinetic study of NK105, a paclitaxel-incorporating micellar nanoparticle formulation. *Br. J. Cancer* **2007**, *97* (2), 170–6.
- (5) Allen, C.; Maysinger, D.; Eisenberg, A. Nanoengineering block copolymer aggregates for drug delivery. *Colloids Surf., B: Interfaces* **1999**, *16*, 3–27.
- (6) Kwon, G. S.; Kataoka, K. Block-Copolymer Micelles as Long-Circulating Drug Vehicles. *Adv. Drug Delivery Rev.* **1995**, *16*, 295–309.
- (7) Harada, A.; Kataoka, K. Supramolecular assemblies of block copolymers in aqueous media as nanocontainers relevant to biological applications. *Prog. Polym. Sci.* **2006**, *31*, 949–82.
- (8) Maeda, H.; Wu, J.; Sawa, T.; Matsumura, Y.; Hori, K. Tumor vascular permeability and the EPR effect in macromolecular therapeutics: a review. *J. Controlled Release* **2000**, *65*, 271–84.
- (9) Matsumura, Y.; Maeda, H. A new concept for macromolecular therapeutics in cancer chemotherapy: mechanism of tumoritropic accumulation of proteins and the antitumor agent smancs. *Cancer Res.* **1986**, *46*, 6387–92.
- (10) Vlerken, L. E.; Amiji, M. M. Multi-functional polymeric nanoparticles for tumour-targeted drug delivery. *Expert Opin. Drug Delivery* **2006**, *3*, 205–16.
- (11) Allen, T. M. Ligand-targeted therapeutics in anticancer therapy. *Nat. Rev. Cancer* **2002**, *2* (10), 750–63.
- (12) Gu, F.; Zhang, L.; Teply, B. A.; Mann, N.; Wang, A.; Radovic-Moreno, A. F.; Langer, R.; Farokhzad, O. C. Precise engineering of targeted nanoparticles by using self-assembled biointegrated block copolymers. *Proc. Natl. Acad. Sci. U.S.A.* **2008**, *105* (7), 2586–91.
- (13) Fang, C.; Shi, B.; Pei, Y. Y.; Hong, M. H.; Wu, J.; Chen, H. Z. In vivo tumor targeting of tumor necrosis factor- α -loaded stealth nanoparticles: effect of MePEG molecular weight and particle size. *Eur. J. Pharm. Sci.* **2006**, *27* (1), 27–36.
- (14) Khalid, M. N.; Simard, P.; Hoarau, D.; Dragomir, A.; Leroux, J. C. Long circulating poly(ethylene glycol)-decorated lipid nanocapsules deliver docetaxel to solid tumors. *Pharm. Res.* **2006**, *23* (4), 752–8.
- (15) McNeeley, K. M.; Annapragada, A.; Bellamkonda, R. V. Decreased circulation time offsets increased efficacy of PEGylated nanocarriers targeting folate receptors of glioma. *Nanotechnology* **2007**, *18*, 1–11.
- (16) Kwon, I. K.; Lee, S. C.; Han, B.; Park, K. Analysis on the current status of targeted drug delivery to tumors. *J. Controlled Release* **2012**, *164* (2), 108–14.
- (17) Kirpotin, D. M.; Drummond, D. C.; Shao, Y.; Shalaby, M. R.; Hong, K.; Nielsen, U. B.; Marks, J. D.; Benz, C. C.; Park, J. W. Antibody targeting of long-circulating lipidic nanoparticles does not increase tumor localization but does increase internalization in animal models. *Cancer Res.* **2006**, *66*, 6732–40.
- (18) Laginha, K. M.; Moase, E. H.; Yu, N.; Huang, A.; Allen, T. M. Bioavailability and therapeutic efficacy of HER2 scFv-targeted liposomal doxorubicin in a murine model of HER2-overexpressing breast cancer. *J. Drug Target.* **2008**, *16*, 605–10.
- (19) Mamot, C.; Drummond, D. C.; Noble, C. O.; Kallab, V.; Guo, Z.; Hong, K.; Kirpotin, D. B.; Park, J. W. Epidermal growth factor receptor-targeted immunoliposomes significantly enhance the efficacy of multiple anticancer drugs in vivo. *Cancer Res.* **2005**, *65*, 11631–8.
- (20) Pirollo, K. F.; Chang, E. H. Does a targeting ligand influence nanoparticle tumor localization or uptake? *Trends Biotechnol.* **2008**, *26*, 552–8.
- (21) Ross, J. S.; Slodkowska, E. A.; Symmans, W. F.; Pusztai, L.; Ravdin, P. M.; Hortobaqi, G. N. The HER-2 receptor and breast cancer: ten years of targeted anti-HER-2 therapy and personalized medicine. *Oncologist* **2009**, *14* (4), 320–68.
- (22) Owens, M. A.; Horten, B. C.; Da Silva, M. M. HER2 amplification ratios by fluorescence in situ hybridization and correlation with immunohistochemistry in a cohort of 6556 breast cancer tissues. *Clin. Br. Cancer* **2004**, *5*, 63–9.
- (23) Harris, A. L.; Nicholson, S.; Sainsbury, J. R. C.; Farndon, J.; Wright, C. Epidermal Growth-Factor Receptors in Breast-Cancer Association with Early Relapse and Death, Poor Response to Hormones and Interactions with Neu. *J. Steroid Biochem. Mol. Biol.* **1989**, *34* (1–6), 123–131.
- (24) Wang, S. L.; Li, Y. X.; Song, Y. W.; Wang, W. H.; Jin, J.; Liu, Y. P.; Liu, X. F.; Yu, Z. H. Triple-negative or HER2-positive status predicts higher rates of locoregional recurrence in node-positive breast cancer patients after mastectomy. *Int. J. Radiat. Oncol. Biol. Phys.* **2011**, *80* (4), 1095–101.
- (25) Slamon, D. J.; Clark, G. M.; Wong, S. G.; Levin, W. J.; Ullrich, A.; McGuire, W. L. Human breast cancer: correlation of relapse and survival with amplification of the HER-2/neu oncogene. *Science* **1987**, *235* (4785), 177–82.
- (26) Baak, J. P.; Chin, D.; van Diest, P. J.; Ortiz, R.; Matze-Cok, P.; Bacus, S. S. Comparative long-term prognostic value of quantitative HER-2/neu protein expression, DNA ploidy, and morphometric and clinical features in paraffin-embedded invasive breast cancer. *Lab. Invest.* **1991**, *64* (2), 215–23.
- (27) Costantini, D.; McLarty, K.; Lee, H.; Done, S. J.; Vallis, K.; Reilly, R. M. Antitumor effects and normal-tissue toxicity of ^{111}In -nuclear localization sequence-trastuzumab in athymic mice bearing HER-positive human breast cancer xenografts. *J. Nucl. Med.* **2010**, *51* (7), 1084–91.
- (28) Fasih, A.; Fonge, H.; Cal, Z.; Leyton, J. V.; Tikhomirov, I.; Done, S. J.; Reilly, R. M. ^{111}In -Bn-DTPA-Nimotuzumab with/without modification with nuclear translocation sequence (NLS) peptides: an auger electron-emitting radioimmunotherapeutic agent for EGFR-positive and trastuzumab (herceptin)-resistant breast cancer. *Br. Cancer Res. Treat.* **2012**, *135* (1), 189–200.
- (29) Hoang, B.; Reilly, R. M.; Allen, C. Block copolymer micelles target auger electron radiotherapy to the nucleus of HER2-positive breast cancer cells. *Biomacromolecules* **2012**, *13*, 455–65.
- (30) Buchegger, F.; Perillo-Adamer, F.; Dupertuis, Y. M.; Delaloye, A. B. Auger radiation targeted into DNA: a therapy perspective. *Eur. J. Nucl. Med. Mol. Imaging* **2006**, *33*, 1352–63.
- (31) Paine, P. L.; Moore, L. C.; Horowitz, S. B. Nuclear envelope permeability. *Nature* **1975**, *254*, 109–114.
- (32) Mikhail, A. S.; Allen, C. Block copolymer micelles for delivery of cancer therapy: transport at the whole body, tissue and cellular levels. *J. Controlled Release* **2009**, *138* (3), 214–23.
- (33) Zeng, F. Q.; Allen, C. Synthesis of Carboxy-Functionalized Heterobifunctional Poly(ethylene glycol) by a Thiol-Anionic Polymerization Method. *Macromolecules* **2006**, *39*, 6391–8.
- (34) Kim, M. S.; Hyun, H.; Cho, Y. H.; Seo, K. S.; Jang, W. Y.; Kim, S. K.; Khang, G.; Lee, H. B. Preparation of methoxy poly(ethyleneglycol)-block-poly(caprolactone) via activated monomer mechanism and examination of micellar characterization. *Polym. Bull.* **2005**, *55*, 149–56.
- (35) Liu, J.; Zeng, F.; Allen, C. In vivo fate of unimers and micelles of a poly(ethylene glycol)-block-poly(caprolactone) copolymer in mice following intravenous administration. *Eur. J. Pharm. Biopharm.* **2007**, *65*, 309–19.
- (36) Zeng, F. Q.; Lee, H.; Allen, C. Epidermal growth factor-conjugated poly(ethylene glycol)-block-poly(delta-valerolactone) copolymer micelles for targeted delivery of chemotherapeutics. *Bioconjugate Chem.* **2006**, *17*, 399–409.
- (37) Lee, H.; Hoang, B.; Fonge, H.; Reilly, R. M.; Allen, C. In vivo distribution of polymeric nanoparticles at the whole-body, tumor, and cellular levels. *Pharm. Res.* **2010**, *27*, 2343–55.
- (38) Hoang, B.; Lee, H.; Reilly, R. M.; Allen, C. Non-invasive monitoring of the fate of ^{111}In -labeled block copolymer micelles by high resolution and high sensitivity microSPECT/CT imaging. *Mol. Pharmaceutics* **2009**, *6*, 581–92.
- (39) Costantini, D.; Chan, C.; Cai, Z.; Vallis, K.; Reilly, R. M. ^{111}In -labeled trastuzumab (herceptin) modified with nuclear localizing sequences (NLS): A novel auger electron-emitting radiotherapeutic agent for HER2/neu-amplified breast cancer. *J. Nucl. Med.* **2007**, *48* (8), 1357–68.
- (40) Schindelin, J.; Arganda-Carreras, I.; Frise, E.; Kaynig, V.; Longair, M.; Pietzsch, T.; Preibisch, S.; Rueden, C.; Saalfeld, S.;

Schmid, B.; Tinevez, J.-Y.; White, D. J.; Hartenstein, V.; Eliceiri, K.; Tomancak, P.; Cardona, A. Fiji: an open-source platform for biological-image analysis. *Nat. Methods* **2012**, *9*, 676–82.

(41) Lee, H.; Fonge, H.; Hoang, B.; Reilly, R. M.; Allen, C. The effects of particle size and molecular targeting on the intratumoral and subcellular distribution of polymeric nanoparticles. *Mol. Pharmaceutics* **2010**, *7*, 1195–208.

(42) Hu, M.; Scollard, D.; Chan, C.; Chen, P.; Vallis, K.; Reilly, R. M. Effect of the EGFR density of breast cancer cells on nuclear importation, in vitro cytotoxicity, and tumor and normal-tissue uptake of [^{111}In]DTPA-hEGF. *Nucl. Med. Biol.* **2007**, *34*, 887–96.

(43) Elbayoumi, T. A.; Torchilin, V. P. Enhanced accumulation of long-circulating liposomes modified with the nucleosome-specific monoclonal antibody 2C5 in various tumours in mice: Gamma-imaging studies. *Eur. J. Nucl. Med. Mol. Imag.* **2006**, *33*, 1196–1205.

(44) Harrington, K. J.; Rowlinson-Busza, G.; Syrigos, K. N.; Uster, P. S.; Abra, R. M.; Stewart, J. S. W. Biodistribution and pharmacokinetics of [^{111}In]DTPA-labelled pegylated liposomes in a human tumour xenograft model: implications for novel targeting strategies. *Br. J. Cancer* **2000**, *83*, 232–238.

(45) Liu, J.; Zeng, F.; Allen, C. In vivo fate of unimers and micelles of a poly(ethylene glycol)-block-poly(caprolactone) copolymer in mice following intravenous administration. *Eur. J. Pharm. Biopharm.* **2007**, *65*, 309–319.

(46) Novakova, K.; Laznicek, M.; Rypacek, F.; Machova, L. I-125-labeled PLA/PEO block copolymer: biodistribution studies in rats. *J. Bioact. Compat. Polym.* **2002**, *17*, 285–296.

(47) Wang, H. E.; Yu, H. M.; Lu, Y. C.; Heish, N. N.; Tseng, Y. L.; Huang, K. L.; Chuang, K. T.; Chen, C. H.; Hwang, J. J.; Lin, W. J.; Wang, S. J.; Ting, G.; Whang-Peng, J.; Deng, W. P. Internal radiotherapy and dosimetric study for [^{111}In]/[^{177}Lu]-pegylated liposomes conjugates in tumor-bearing mice. *Nucl. Instrum. Methods* **2006**, *569*, 533–537.

(48) Tang, Y.; Scollard, D.; Chen, P.; Wang, J.; Holloway, C.; Reilly, R. M. Imaging of HER2/neu expression in BT-474 human breast cancer xenografts in athymic mice using [$^{99\text{m}}\text{Tc}$]-HYNICTrastuzumab (Herceptin) Fab fragments. *Nucl. Med. Commun.* **2005**, *26*, 427–432.

(49) Cabral, H.; Matsumoto, Y.; Mizuno, K.; Chen, Q.; Murakami, M.; Kimura, M.; Terada, Y.; Kano, M. R.; Miyazono, K.; Uesaka, M.; Nishiyama, N.; Kataoka, K. Accumulation of sub-100 nm polymeric micelles in poorly permeable tumours depends on size. *Nat. Nanotechnol.* **2011**, *6*, 815–23.

(50) Hu, Q.; Gu, G.; Liu, Z.; Jiang, M.; Kang, T.; Miao, D.; Tu, Y.; Pang, Z.; Song, Q.; Yao, L.; Xia, H.; Chen, H.; Jiang, X.; Gao, X.; Chen, J. F3 peptide-functionalized PEG-PLA nanoparticles co-administrated with tLyp-1 peptide for anti-glioma drug delivery. *Biomaterials* **2013**, *34*, 1135–45.

(51) Jiang, X.; Xin, H.; Gu, J.; Xu, X.; Xia, W.; Chen, S.; Xie, Y.; Chen, L.; Chen, Y.; Sha, X.; Fang, X. Solid tumor penetration by integrin-mediated pegylated poly(trimethylene carbonate) nanoparticles loaded with paclitaxel. *Biomaterials* **2013**, *34*, 1739–46.

(52) Kano, M. R.; Bae, Y.; Iwata, C.; Morishita, Y.; Oka, M.; Fujii, T.; Komuro, A.; Kiyono, K.; Kaminishi, M.; Hirakawa, K.; Ouchi, Y.; Nishiyama, N.; Kataoka, K.; Miyazono, K. Improvement of cancer-targeting therapy, using nanocarriers for intractable solid tumours by inhibition of TGF- β signaling. *Proc. Natl. Acad. Sci. U.S.A.* **2007**, *104*, 3460–5.

(53) Gillies, R. J.; Schornack, P. A.; Secomb, T. W.; Raghunand, N. Causes and effects of heterogeneous perfusion in tumors. *Neoplasia* **1999**, *1* (3), 197–207.

(54) Penault-Llorca, F.; Adelaide, J.; Houvenaeghel, G.; Hassoun, J.; Birnbaum, D.; Jacquemier, J. Optimization of immunohistochemical detection of ERBB2 in human breast cancer: impact of fixation. *J. Pathol.* **1994**, *173*, 65–75.

(55) Subik, K.; Lee, J.-F.; Baxter, L.; Strzepek, T.; Costello, D.; Crowley, P.; Xing, L.; Hung, M.-C.; Bonfiglio, T.; Hicks, D. G.; Tang, P. The expression patterns of ER, PR, HER2, CK5/6, EGFR, Ki-67 and AR by Immunohistochemical analysis in breast cancer cell lines. *Breast Cancer (Auckl)* **2010**, *4*, 35–41.

(56) Jain, R. K.; Stylianopoulos, T. Delivering nanomedicine to solid tumors. *Nat. Rev. Clin. Oncol.* **2010**, *7* (11), 653–64.

(57) Chauhan, V. P.; Stylianopoulos, T.; Boucher, Y.; Jain, R. K. Delivery of molecular and nanoscale medicine to tumors: transport barriers and strategies. *Annu. Rev. Chem. Biomol.* **2011**, *2*, 281–98.

(58) Pante, N.; Kann, M. Nuclear pore complex is able to transport macromolecules with diameters of ~ 39 nm. *Mol. Biol. Cell* **2002**, *13*, 425–34.

(59) Misra, R.; Sahoo, S. K. Intracellular trafficking of nuclear localization signal conjugated nanoparticles for cancer therapy. *Eur. J. Pharm. Sci.* **2010**, *39*, 152–63.

(60) Yu, J.; Xie, X.; Zheng, M.; Yu, L.; Zhang, L.; Zhao, J.; Jiang, D.; Che, X. Fabrication and characterization of nuclear localization signal-conjugated glycol chitosan micelles for improving the nuclear delivery of doxorubicin. *Int. J. Nanomed.* **2012**, *7*, 5079–90.

(61) Aronov, O.; Horowitz, A. T.; Gabizon, A.; Fuentes, M. A.; Perez, J. M.; Gibson, D. Nuclear localization signal-targeted poly(ethylene glycol) conjugates as potential carriers and nuclear localizing agents for carboplatin analogues. *Bioconjugate Chem.* **2004**, *15* (4), 814–23.

(62) Sethuraman, V. A.; Bae, Y. TAT peptide-based micelle system for potential active targeting of anti-cancer agents to acidic solid tumors. *J. Controlled Release* **2007**, *118* (2), 216–24.

(63) Symens, N.; Soenen, S. J.; Rejman, J.; Braeckmans, K.; DeSmedt, S. C.; Remaut, K. Intracellular partitioning of cell organelles and extraneous nanoparticles during mitosis. *Adv. Drug Delivery Rev.* **2012**, *64*, 78–94.

(64) Fenton, B. M.; Paoni, S. F.; Lee, J.; Koch, C. J.; Lord, E. M. Quantification of tumour vasculature and hypoxia by immunohistochemical staining and HbO $_2$ saturation measurements. *Br. J. Cancer* **1999**, *79* (3–4), 464–71.

(65) Reilly, R. M.; Kiarash, R.; Cameron, R. G.; Porlier, N.; Sandhu, J.; Hill, R. P.; Vallis, K.; Hendler, A.; Gariepy, J. [^{111}In]-Labeled EGF is selectively radiotoxic to human breast cancer cells overexpressing EGFR. *J. Nucl. Med.* **2000**, *41*, 429–438.

(66) Chen, T. J.; Cheng, T. H.; Chen, C. Y.; Hsu, S. C.; Cheng, T. L.; Liu, G. C.; Wang, Y. M. Targeted herceptin-dextran iron oxide nanoparticles for noninvasive imaging of HER2/neu receptors using MRI. *J. Biol. Inorg. Chem.* **2009**, *14* (2), 253–60.

(67) Wang, Y.; Liu, X.; Nakamura, K.; Chen, L.; Rusckowski, M.; Hnatowich, D. Improving in vivo delivery of antisense MORF using Herceptin/streptavidin nanoparticle. *Eur. J. Nucl. Med. Mol. Imag.* **2009**, *36* (12), 1977–86.